Electronic Supplemental Information

Microfluidic-based Solid Phase Extraction of Cell Free DNA

Camila D.M. Campos,[a,b] Sachindra S. T. Gamage,[a,b] Joshua M. Jackson, [a,b]

Malgorzata A. Witek, [a,b,c] Daniel S. Park [b,d] , Michael C. Murphy [b,d], Andrew K. Godwin,[e]

and Steven A. Soper [a,b,e,f,g,h]

[a] Department of Chemistry, University of Kansas, Lawrence, KS, USA
[b] Center of Biomodular Multi-scale Systems for Precision Medicine
[c] Department of Biomedical Engineering, The University of North Carolina, Chapel Hill, NC 27599
[d] Department of Mechanical Engineering, Louisiana State University, Baton Rouge, LA
[e] University of Kansas Cancer Center, University of Kansas Medical Center, Kansas City, KS, USA
[f] BioEngineering Program, The University of Kansas, Lawrence, KS 66047
[g] Department of Mechanical Engineering, The University of Kansas, Lawrence, KS 66047
[h] Ulsan National Institute of Science and Technology, Ulsan, Republic of Korea

[a] Department of Chemistry, University of Kansas, Lawrence, KS, USA
[b] Center of Biomodular Multi-scale Systems for Precision Medicine
[c] Department of Biomedical Engineering, The University of North Carolina, Chapel Hill, NC 27599
[d] Department of Mechanical Engineering, Louisiana State University, Baton Rouge, LA
[e] University of Kansas Cancer Center, University of Kansas, Kansas City, KS, USA
[f] BioEngineering Program, The University of Kansas, Lawrence, KS 66047
[g] Department of Mechanical Engineering, The University of Kansas, Lawrence, KS 66047
[h] Ulsan National Institute of Science and Technology, Ulsan, Republic of Korea

Table of contents

List of Figures

List of Tables

1. cfDNA SPE workflow of commercial kits

The diagram in Fig. S1 presents the steps typically employed to extract cfDNA from clinical samples using commercial kits. Each box is an operation that in many cases is carried out manually, and therefore prone to operator error. As an example on how the pre-analytics can affect the reproducibility of the cfDNA extraction, we cite the SPIDIA-DNAplas study[1] that reported variations in the amount (mass) of cfDNA isolated from the same sample of two orders of magnitude from >50 different laboratories.
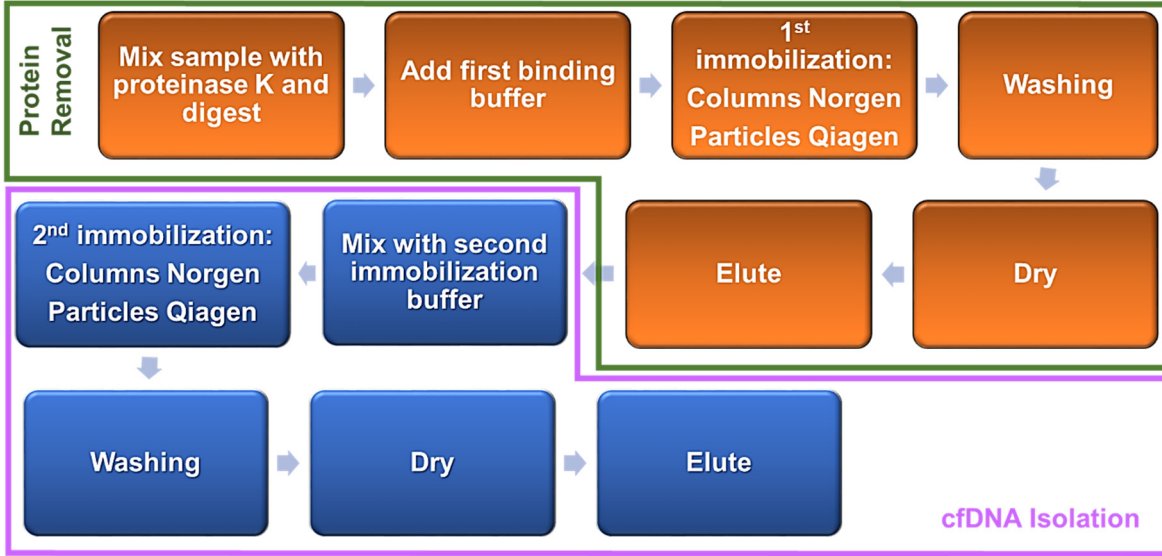
Fig. S1. Protocol for extraction of cfDNA using commercial kits. In this workflow, the input is plasma that has been isolated from whole blood using centrifugation.

2. Monte Carlo simulation of DNA recovery

Diffusion dynamics in the Monte Carlo simulations of cfDNA recovery. To model the µSPE of cfDNA, we implemented a Monte Carlo simulation that accounts for the diffusive and convective transport of cfDNA to the µSPE surfaces and the probability of µSPE binding to the surface once a surface interaction begins. The delivery of cfDNA to the µSPE surface is limited by diffusion through the immobilization buffer. As the sample is hydrodynamically pumped through the device, cfDNA diffuses laterally and longitudinally according to Fick's Second Law. Over a small time increment, Δt, the probability that the cfDNA will diffuse a distance x_D from its initial position is given by a Gaussian distribution, $P(x)$, which has a standard deviation of $\sigma = \sqrt{2D\Delta t}$ where D is the cfDNA diffusion coefficient and can be calculated using:

$$P(x) = \frac{1}{\sigma\sqrt{2\pi}}e^{-\frac{x_D^2}{2\sigma^2}} \qquad \text{(Eq. S1)}$$

In addition to diffusive transfer, the cfDNA experiences Poiseuille flow. In a high aspect ratio microchannel with a width of W, the cfDNA forward velocity at position x from the channel's midline can be approximated by;

$$V(x) = 1.5\, V_{ave}\left(1 - \left(\frac{x}{w/2}\right)\right)^2 \quad \text{(Eq. S2)}$$

where V_{ave} is calculated by dividing the volumetric flow rate by the microfluidic bed's cross-section. The consequences of the parabolic flow profile in Eq. S2 are complex. As the cfDNA diffuses closer to the µSPE surfaces, forward motion slows, and more time is given for diffusion to occur. Consequently, the residence time

of different cfDNA molecules within the same device will not be the same if they take different diffusive, random paths through the chip, which follows Poiseuille flow.

Thus, we developed a Monte Carlo simulation to simulate the flow path of individual cfDNA molecules through µSPE devices when the convective flow was driven hydrodynamically, then repeat this process until the averaged cfDNA recovery converges. This model enables testing various µSPE bed lengths, inter-pillar spacings (W), and average flow velocities (V_{ave}) to design µSPE architectures with high recovery, high throughput, and high cfDNA loads.

For each cfDNA molecule, the Monte Carlo propagates the cfDNA axial position (X dimension) and longitudinal position (Y dimension) over finite time steps (Δt):

$$x(t) = x(t - \Delta t) + rand(P(\sigma(D, \Delta t))) \qquad \text{(Eq. S3a)}$$
$$y(t) = y(t - \Delta t) + V\big(x(t - \Delta t)\big) + rand(P(\sigma(D, \Delta t))) \qquad \text{(Eq. S3b)}$$

In Eq. S3a, the cfDNA lateral x position changes with axial diffusion over Δt using $rand(P(\sigma(D, \Delta t)))$, which is given by a pseudo-random number generator that moves the cfDNA laterally according to a Gaussian $P(x)$ distribution with standard deviation σ. Longitudinal diffusion is considered in the same manner by Eq. S3b, but the cfDNA has an additional term due to Poiseuille flow, namely the $V\big(x(t - \Delta t)\big)$ term described in Eq. S2.

As the position of a cfDNA molecule propagates according to Eqs. S3, the cfDNA could interact with the µSPE surface's (i.e., $x = \pm W/2$), at which point SPE could take place. The probability of SPE, P_{SPE}, was varied within the simulations to match empirical data, as described below.

Implementation of physical dynamics into Monte Carlo model and model validation. The flow profile through an µSPE bed with length L_{bed} experienced by a cfDNA molecule was approximated as a straight microfluidic channel with a width W equal to the interpillar spacing and length $L = L_{bed}C$, where C is a correction factor linked to elongation of the flow path due to the pillars' geometry. For diamond micropillars, $C = \sqrt{2} \approx 1.41$, and for circular micropillars, $C = \pi/2 \approx 1.57$.[2] cfDNA molecules were initiated at 11 positions along the pseudo-channel's midline and the cfDNA position was propagated by Eqs. S3. Upon surface interaction, the cfDNA was propagated by multiplying $V(x)$ (Eq. S2) by the simulation's time step Δt, and the probability of SPE was assessed by using a pseudo-random number generator uniformly distributed between 0 and 1. If the random number was less than P_{SPE}, the cfDNA was recovered. If not, the molecule's position was propagated further via Eq. S3. This series of events continued until either the cfDNA was extracted or the cfDNA exited the µSPE bed ($y = L$).

Each cfDNA track was a binary event, extracted or exited, and thousands of cfDNA molecules were tracked until the simulated extraction converged, defined herein as a <0.01% change in average extraction when additional molecules were tracked. An additional convergence criterion was emplaced that stipulated a <10% standard deviation for five repetitive simulations. Lastly, given that various V_{ave} were tested, the program's discretization of time into Δt time steps were added as a final convergence criterion; after halving the Δt increment, the averaged solution from five simulations must differ by <1%, else the simulations would be repeated after halving Δt again.

Matching µSPE probability to empirical data and effects of µSPE design on cfDNA extraction. The Monte Carlo simulations used the cfDNA properties shown in Table S1. The diffusion constant of a 122 bp cfDNA was estimated for aqueous solutions via the power law relationship provided by Stellwagen, *et al.*[3] and was scaled down for the immobilization buffer's increased viscosity, as measured in house.

Table S1. Parameters used for cfDNA SPE simulations. Note that immobilization buffer viscosity was obtained with a pressure sensor and capillary tubing using differential fluidic resistance measurements against PBS, and the immobilization buffer viscosity was used to scale down the cfDNA's aqueous diffusion constant for simulated diffusion dynamics.

Property	Value
cfDNA length	122 bp
PBS viscosity	1.00 ±0.05 cP
Viscosity after mix with IB	4.31 ±0.13 cP
Diffusion constant, aqueous	30.6 μm^2/s (Stellwagen, et al. [3])
Diffusion constant, immobilization buffer (D)	7.1 μm^2/s

The first set of simulations sought to adjust the unknown probability of SPE per surface interaction (P_{SPE}) to match empirical data. For µSPE devices with 35 µm inter-pillar spacing, 24 mm bed length, path length adjustment for circular pillars (effective length of 37.7 mm), and either 0.6 mm/s or 1.5 mm/s linear velocity, we varied P_{SPE} and obtained the average cfDNA recovery from the Monte Carlo simulations. A diffusion-limited regime was apparent at high P_{SPE}, evident by little change in cfDNA recovery with decreasing P_{SPE}, and a reaction-limited regime at low P_{SPE}, where slight changes in P_{SPE} drastically changed cfDNA recovery. Best fit to the empirical data was found for 2% P_{SPE} (2% of surface interactions yielded SPE extraction). At 2% P_{SPE}, the recovery at 0.6 mm/s remained diffusion-limited (92% simulated recovery vs. 92% empirically). At 1.5 mm/s, reduced residence times available for diffusion shifted the reaction-limited transition to higher P_{SPE} values, where it became more critical that the less frequent surface interactions were successful to maintain high cfDNA extraction (56% simulated vs. 59% empirically). After establishing the probability of SPE within the Monte Carlo simulation, we tested the effect of inter-pillar spacing on cfDNA extraction (see Fig. 1 in the main paper).

3. Patient information

Table S2. Patient clinical information. Plasma contained in EDTA tubes were secured from each of these patients.

Patient ID/Year Collected	Histology Confirmation	Gender/Race	*KRAS* status
21000/ 2016	adenocarcinoma of colon, metastatic	Female/ White	G12V:GGT>GTT
21019/ 2016	adenocarcinoma of colon, metastatic	Male/ White	not detected
21957/ 2016	adenocarcinoma of colon, localized	Male/ White	not Detected
22282/ 2016	adenocarcinoma of colon, localized	Male/ White	not Detected
22327/ 2017	adenocarcinoma of colon, metastatic	Female/ White	not Detected
18697/ 2017	adenocarcinoma of the lung, metastatic (non-small cell lung cancer (NSCLC)	Female / Black or African American	not detected
28775/ 2017	adenocarcinoma of the lung, localized non-small cell lung cancer (NSCLC)	Female/White	not tested
16180/ 2017	adenocarcinoma of lung, metastatic non-small cell lung cancer (NSCLC)	Male/White	G13D

4. PCR and quantitative (qPCR)

Amplified DNA fragments (122 bp and 290 bp) were spiked in plasma of healthy donors to emulate the typical concentration of cfDNA in cancer patients' plasma. The amplicons were produced and quantified using primers that target a region within the *KRAS* gene. The primers' sequences are listed in Table S3. Amplicons were produced via PCR with a cocktail consisting of an initial denaturation step at 94°C for 3 min followed by 40 cycles of the following: 94°C for 30 s, 55°C for 15 s, 72°C for 30 s, with a final extension at 72°C for 3 min. After amplification, samples were purified using a QIAquick® PCR purification kit (Qiagen), following the supplier's protocol. qPCR was used to assess the amount of isolated cfDNA using SsoAdvanced™ Universal SYBR® Green Supermix. Two µL of the eluent was used in 10 µL reaction with 0.25 µM reverse and forward primers. Fig. S2A shows the amplification curves obtained by qPCR for different amounts of the 122 bp model cfDNA fragment.

Table S3. Primers employed for PCR to generate 122 bp and 290 bp *KRAS* fragments from HT29 cells. These fragments were used as models to quantify cfDNA recovery using the µSPE. Also shown are primers used to amplify a section of the GAPDH and 18S genes in the same cell lines.

	PCR (5'→3')	
Gene	Forward	Reverse
KRAS – 122 bp	GCCTGCTGAAAATGACT	CTCTATTGTTGGATCATATTCG
KRAS – 290 bp	TTAAAAGGTACTGGTGGAGTATTTGA	AAAATGGTCAGAGAAACCTTTATCTG
GAPDH	GGTGTGAACCATGAGAAAGTATGA	GAGTCCTTCCACGATACCAAAG
18S	GTAACCCGTTGAACCCCATT	CCATCCAATCGGTAGTAGCG

18S and *GAPDH* sequences (Table S3) were used to quantify the amount of cfDNA extracted from healthy donors and cancer patients (qPCR amplification curves for *18S* are presented in Fig. S2A) owing to their high abundance in the genome and their use as housekeeping genes to allow for qPCR quantification.
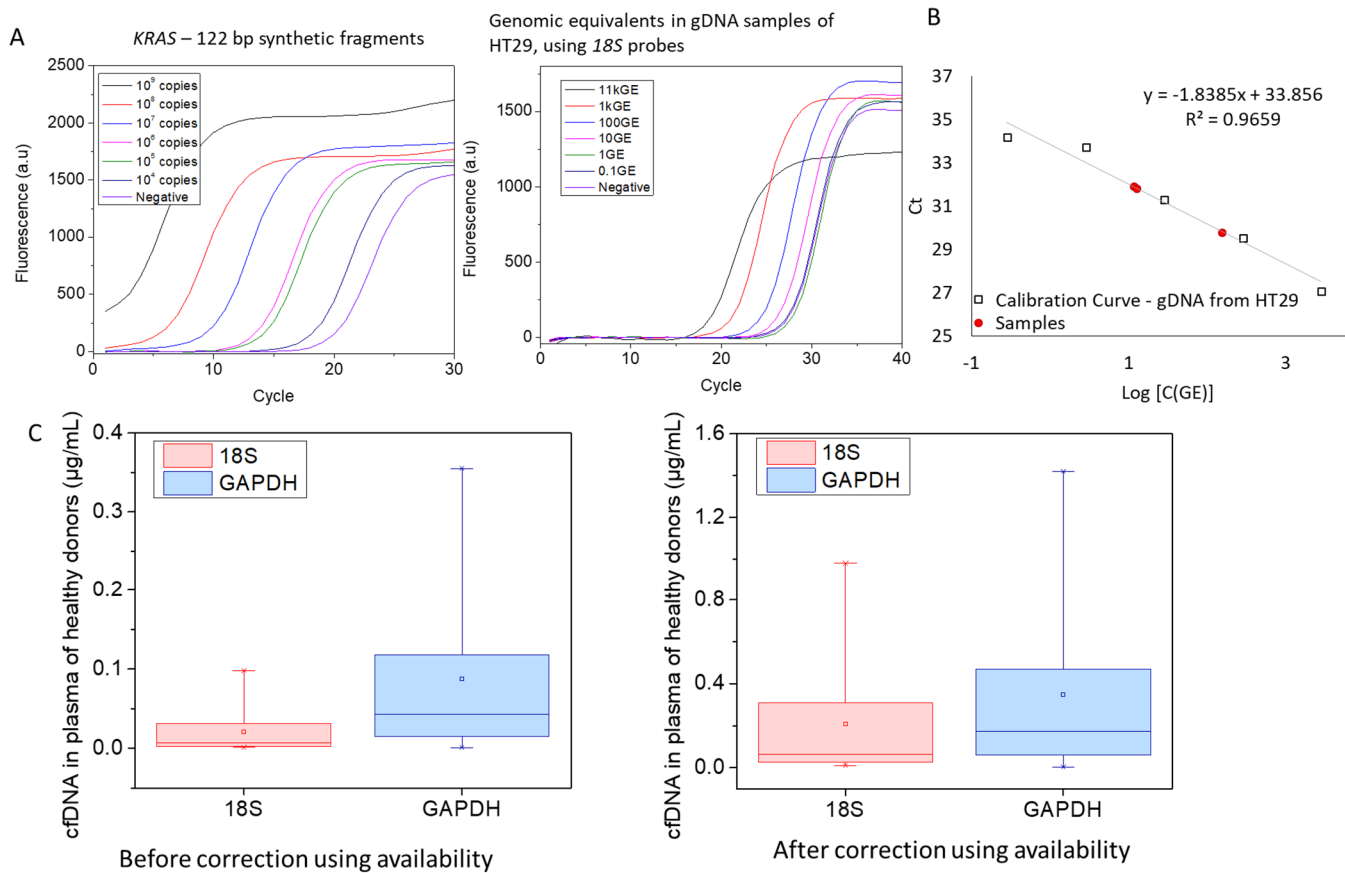

Fig. S2. A) PCR amplification curves for *KRAS* (122 bp) and gDNA extracted from HT29 cells, and probing for the 18S sequence. B) Critical cycle vs. log concentration in genome equivalents for gDNA extracted from HT29 cells, which was used as the reference and for samples extracted using µSPE. C) Results for healthy donors before and after correction for availability.

When quantifying the levels of cfDNA in the same set of samples, for example when using *GAPDH* and *18S* as target sequences (Fig. S2A, B), we observed significant differences (p = 0.0053) in the amount of cfDNA detected (Fig. S2C shows this effect in healthy donor samples). This discrepancy is not due to amplification inefficiency, but is the result of small cfDNA fragments that are present in plasma that reduces the number of copies of an intact gene, and thus unavailable for amplification due to the inability to properly prime the PCR.[4] The unavailability is proportional to the size of the amplicons, as demonstrated by Horlitz *et al.*[4]

Correcting for availability using Eq. S4[4] eliminated the differences in quantification of cfDNA assessed in plasma of healthy donors using *GAPDH* or *18S* (Fig. S2C; after correction, p = 0.09894). In Eq. S4, <u>amplicon</u> and <u>fragments</u> are the sizes of the amplicon (151 bp for *18S* and 121 bp for *GAPDH*) and the isolated fragments (167 bp for cfDNA and >60 kbp for gDNA).

$$GE_{Nominal} = \frac{GE_{Measured}}{(1-amplicon/fragment)} \quad \text{(Eq. S4)}$$

5. Ligase Detection Reaction (LDR) analysis.

LDR analyses were performed using the primers listed in Table S4. The target mutations chosen were the most common based on data available at the COSMIC database[5] (Fig. S3). Together, they encompass 78% of the *KRAS* mutation cases in NSCLC and 86% in CRC (see Fig. 6 in the main paper).

The LDR was performed with 0.4 ng of DNA and 4 nM each discriminating and common primers (Table S4) and 4 units of Taq Ligase enzyme. The LDR mix was preheated to 94°C for 2 min following 25 cycles using the following temperatures: 94°C for 30 s; 54°C for 4 min.

Table S4. Primers sequences used in LDR to detect point mutations in the *KRAS* gene.

| DNA Site	Discriminating primer 5' - 3'	Common primer 5' – 3' Cy5	Ligation product size (nt)
c.34.WT	TTTTTTTTTTTTTTTTTATATAAACTTGTGGTAGTTGGAGCTG (43 nt)	**p**GTGGCGTAGGCAAGAGTGCCAA (22 nt)	65
G12S (c.34G>A)	TTTTCTGAATATATAAACTTGTGGTAGTTGGAGCTA (36 nt)		58
c.35.WT	TTTTTTTTTTTTTTTTTATATAAACTTGTGGTAGTTGGAGCTGG (44 nt)	**p**TGGCGTAGGCAAGAGTGCCTT (21 nt)	65
G12D (c.35G>A)	TTTTTTTTTTTATATAAACTTGTGGTAGTTGGAGCTGA (38 nt)		59
G12V (c.35G>T)	TTTATATAAACTTGTGGTAGTTGGAGCTGT (30 nt)		51
c.38.Wild	TTTTTTTTTTTTTTTTTATATAAACTTGTGGTAGTTGGAGCTGGTGG (47 nt)	**p**CGTAGGCAAGAGTGCCTTGAC (21 nt)	68
G13D (c.38G>A)	TTTTTTTTTTTATATAAACTTGTGGTAGTTGGAGCTGGTGA (41 nt)		62

p- Freshly phosphorylated
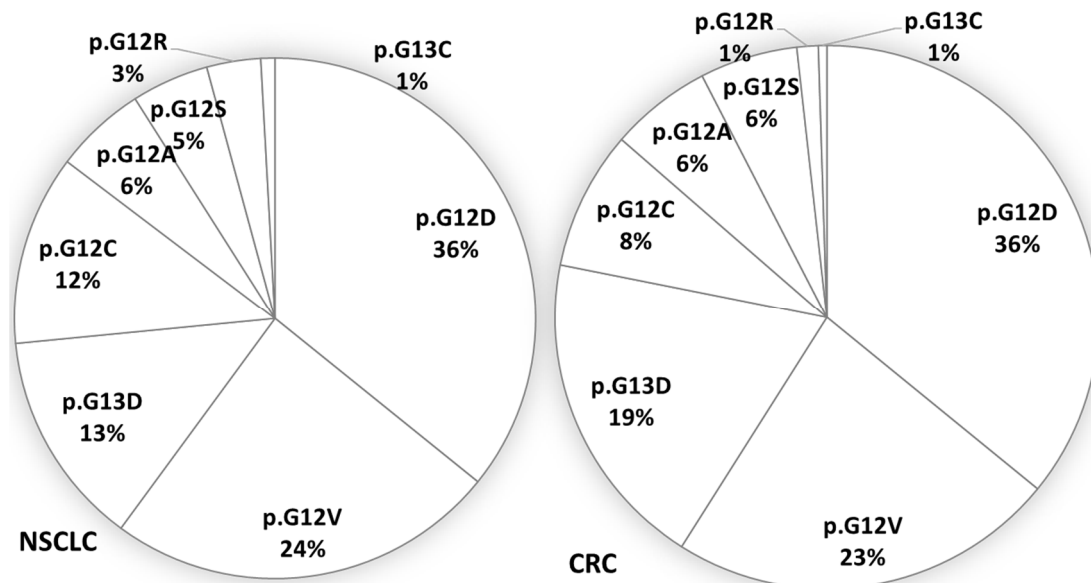
Fig. S3. Pie chart presenting the most common *KRAS* mutations in NSCLC and CRC according to the cosmic database (https://cancer.sanger.ac.uk/cosmic).

6. Fabrication of the mold for 24-bed µSPE devices

A clear-field photomask was fabricated to manufacture a SU8 scaffold. The scaffold was used to make a NiCo mold for hot embossing or injection molding of the 24-bed µSPE device with high load (Fig S5.a,b). Optical lithography was carried out with SU8 photoresist (Microchem, Inc., Newton, MA) on a Si substrate with the photomask. The Si substrate was coated with Cr (20 nm)/Au (50 nm)/Cr (20 nm) by an e-beam evaporator. The first Cr layer served to improve the adhesion of Au to the Si substrate, the Au layer acts as a seed layer for electroforming, and the last Cr layer was used to provide good adhesion with SU8. Spin-coating of SU8 2010 was done at 500 rpm for 30 s, followed by pre-baking. The measured thickness of SU8 after pre-baking was ~40 µm. Flycutting was used to reduce the thickness of the spin-coated SU8 to the desired value (10 µm). The flycut SU8 samples were baked at 65°C for 1 h to smooth out the flycutting tool traces. Then, UV exposure of the SU8 samples was performed. Several UV exposure doses were tested to obtain reliable formation of the pillar array pattern. During the UV exposure, an UV filter was used to filter out the UV wavelengths below 350 nm due to the high sensitivity of SU8 at wavelengths below 350 nm. Also, a vacuum contact was used to realize intimate contact between the photomask and the SU8 film. After UV exposure, post exposure baking (PEB) was used to crosslink the exposed SU8. Development of the SU8 samples was done in SU8 developer for the specified time (supplier's protocol) for each SU8 thickness, followed by rinsing with isopropanol and drying in air. Hard baking at 150°C for 5 min improved the adhesion of the pillar arrays and was followed by plasma cleaning using 100% oxygen. The top Cr layer was etched in a Cr etchant (a solution of 20 g: 20 g: 100 ml of $NaOH:K_3Fe(CN)_6:H_2O$)) to expose the Au seed layer for electroforming. Microscope inspection results are shown in Fig. S5C, D. SEM inspection was done to evaluate the quality of the SU8 pillar arrays, as shown in Fig. S5E. The SU8 pillar arrays had vertical sidewalls, which will facilitate micromolding.
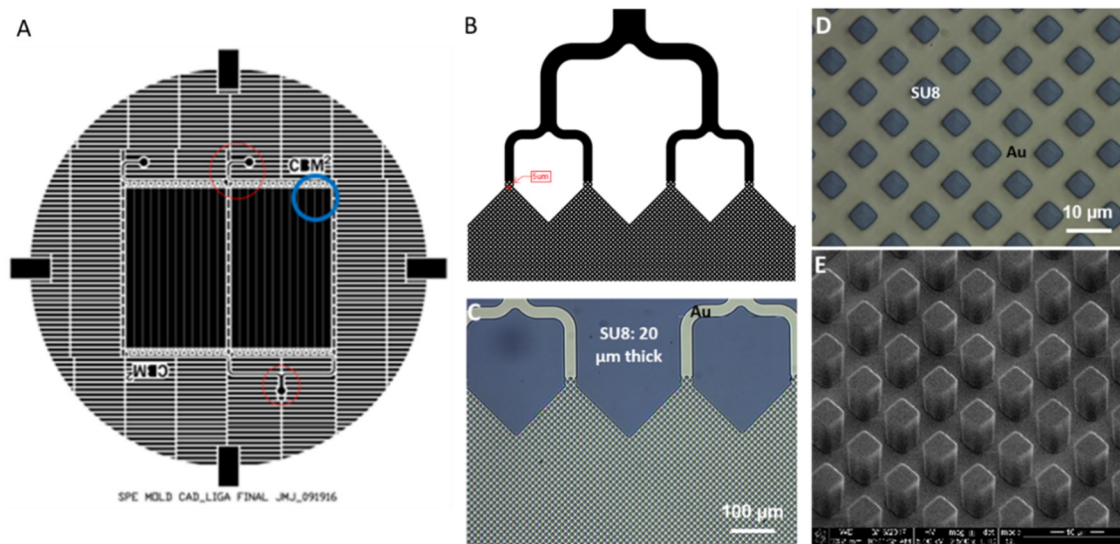
Fig. S4. (A)The overall design view of the µSPE with red circles pointing to chip outlet and (B) close-up view from the blue circle in (A) with 5 µm by 5 µm pillar arrays. (C) Microscope images from the region shown in (B). (D) Microscope images for a close-up view from (C). (E) SEM images of pillar arrays.

Electroforming of NiCo was carried out at NiCoForm Co. (USA). NiCo was chosen instead of Ni because of its higher tensile strength, higher hardness, and better corrosion resistance compared to Ni. Electroforming of NiCo filled the SU8 pillar arrays from the bottom of the gold seed layer. Once NiCo reached the top of the SU8 pillar arrays, electroforming was continued to produce a NiCo base thickness of about 1.5 mm. The uneven backside of the NiCo samples were machined to obtain flat backsides with a final base thickness of 1.0 mm. The Si substrate was removed in KOH solution. The exposed metal seed layers of chromium and gold were removed in the corresponding metal etchants. SU8 removal in the NiCo mold was performed using a microwave plasma asher (300 series MW plasma system, PVA Tepla America, Inc.) using 75% O_2 and 25% CF_4 at a working pressure 760 mTorr and a power of 500 Watts.

After removal of the SU8, each NiCo sample was treated with a proprietary thermal process (NiCoForm, USA) to relieve stress to a specified flatness over the patterned area of the mold. The flatness of the NiCo molds was evaluated by optical profilometry (Nanovea ST400, Micro Photonics Inc., USA) after the thermal relief process. Each NiCo sample was waterjet cut into an 85 mm diameter circular shape. A stainless steel (SS 316) fixture with a circular cavity was cut by waterjet for each NiCo sample to be mounted in. Several through-holes were made inside the cavities so that the NiCo samples could be mounted and laser welded (Mezzo Technologies, Inc., USA) into the stainless steel fixtures. Laser welding completed the fabrication of the NiCo molds, which can be used for micromolding of polymers using either hot embossing or injection molding.

7. Replication of High density pillar arrays in PC and COC

For the fabrication of 24-bed devices, the choice of material for replication is particularly important. It needs to fulfill the following requirements: (i) Support µSPE of cfDNA in the presence of the IB; and (ii) provide good replication characteristics. Both COC and PC can be used for µSPE, as no statistical difference in amount of extracted cfDNA was observed for spike in experiments.

In terms of moldability, PC has high impact-resistance and can undergo large deformations/stress without cracking or breaking. The tensile strength of PC is 65-70 N/mm² while for COC it is 46–63 N/mm². Higher tensile strength represents an advantage during molding especially when fabricating fine structures; high aspect ratio and/or small dimensions. Although we did not experience difficulties in molding COC devices with pillars ranging in size from 60-100 µm, it was a challenge with ~6 µm pillars (Fig. S5A-B). For larger pillars, such as the ones found on the chips with 1 or 3 beds, the mechanical properties of COC do not result in failure or lower quality,

as long as the process is controlled with a precision of ±2°C for the molding or demolding temperatures. If the device is demolded at higher temperatures, the polymer is not fully solidified and pillar elongation (pulling) will be observed. If the polymer is cooled too much, the polymer becomes too hard, and more prone to breaking due to the traction produced during the demolding.

Replication in PC produced better fidelity (Fig. S5C-D). One reason for the better results observed when the devices were embossed in this case using PC is the lower adhesion of the polymer to the mold master. When polymer adheres to the mold master, pillars are pulled during the demolding creating a traction force acting on the pillars. As COC is more adherent than PC, the traction is stronger for the former. At the same time, COC is also more fragile, so the pillars tend to break more easily due to this traction. As a result, a large number of pillars embossed in COC were broken or elongated after demolding (Fig. S5A, B), which did not appear to happen when PC was used (Fig. S5C-D).
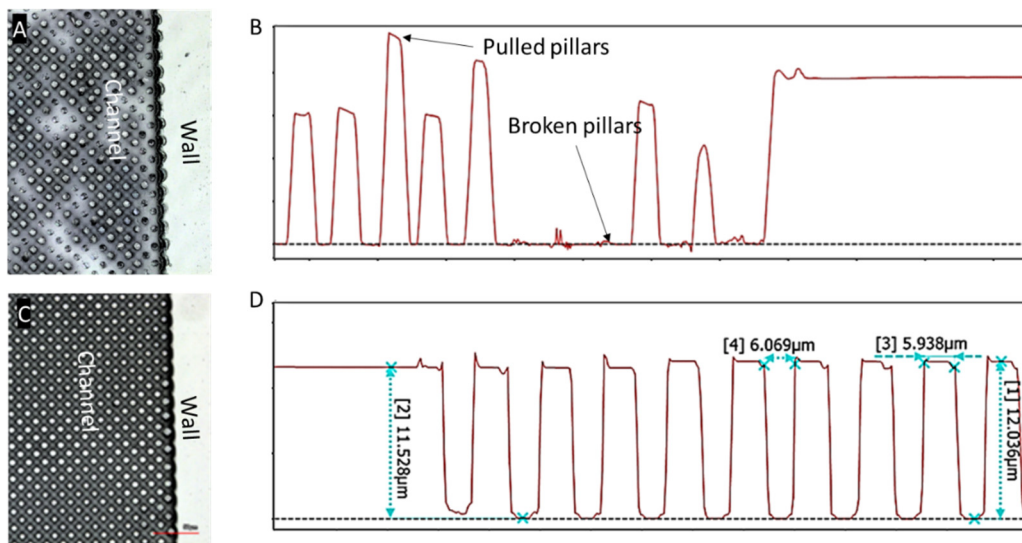

Fig. S5. (A) Image of the 24-bed device embossed in COC with defects formed during demolding, (B) profilometry data showing the missing pillars. (C) Image of the device embossed in PC and (D) profilometry.
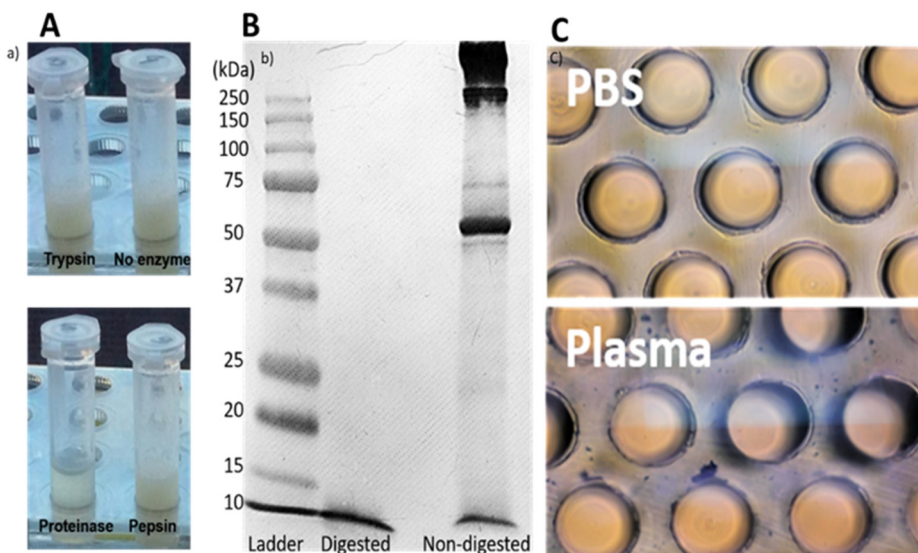
8. Plasma Protein Digestion

Fig. S6. (A) Picture of the product of enzymatic digestion of plasma mixed with immobilization buffer - 17% PEG and 10 mM MgCl2, prepared in an EtOH solution. (B) SDS-PAGE gel electrophoresis of the products of plasma digestion by proteinase K and comparison with a non-proteinase K digestion of a plasma sample. (C) Protein precipitation inside the device was confirmed by staining with Coomassie blue.

To assess the precipitation of protein inside the µSPE device, after cleaning the device with EtOH and drying with air, Coomassie blue staining solution (0.1% Coomassie blue (Biorad), 50% methanol and 10% Acetic acid) was injected into the device and allowed to react for 20 min. After the reaction, the staining solution was removed from the microfluidic device using another EtOH wash. Images were acquired using a Nikon Eclipse TE300 microscope. Fig. S6 shows these results.

References
1. F. Malentacchi, S. Pizzamiglio, P. Verderio, M. Pazzagli, C. Orlando, C. M. Ciniselli, K. Günther and S. Gelmini, *Clinical Chemistry and Laboratory Medicine*, 2015, 53, 1935-1942.
2. K. N. Battle, J. M. Jackson, M. A. Witek, M. L. Hupert, S. A. Hunsucker, P. M. Armistead and S. A. Soper, *The Analyst*, 2014, 139, 1355-1363.
3. E. Stellwagen, Y. Lu and N. C. Stellwagen, *Biochemistry*, 2003, 42, 11745-11750.
4. M. Horlitz, A. Lucas and M. Sprenger-Haussels, *PLoS One*, 2009, 4, e7207.
5. COSMIC, COSMIC - Catalogue of Somatic Mutations in Cancer, https://cancer.sanger.ac.uk/cosmic, Accessed 01-Mai-2018, 2018.